Volume 1 | Number 1 | Jan 2013 | Pages 1–100

Journal of
Materials Chemistry A

Materials for energy and sustainability
www.rsc.org/materialsA

ROYAL SOCIETY
OF CHEMISTRY

ROYAL SOCIETY
OF CHEMISTRY

www.rsc.org/materialsA

Journal of Material Chemistry A

PAPER

Hydrogen-Bonding-Mediated Structural Stability and Electrochemical Performance in Iron Fluoride Cathode Materials

Zuosheng Li, Beizhou Wang, Chilin Li, Jianjun Liu*, Wenqing Zhang

Numerous lithium ions battery cathode materials containing trace amounts of water accommodated in Li^+ transportation tunnels have been experimentally synthesized. However, the impact of water on structural stability and electrochemical performance of cathode materials is still unclear so far. Here, the first-principles calculations combining thermodynamics analysis for $Li_xFeF_3 \bullet 0.33H_2O$ were performed to unravel interaction mechanism among framework FeF_3, H_2O, and Li^+. The FeF_3 framework structure distortion is mitigated by hydrogen bonding between isolated H_2O and F^- ions, bringing opposite effects in stability of hydrogen bonding and instability of structural distortion. The hydrogen bonding strength of $F^- \cdots H_2O$ can further be mediated by the Li^+-inserted amount, which indirectly results in a wide discharge voltage window from 2.2 to 3.6V. Li^+ transportation barrier in cooperative mode is also tuned by the flexible hydrogen bonding strength due to different occupied positions. $Li_{0.66}FeF_3 \bullet 0.33H_2O$ is determined as the most stable species and more Li^+ insertion directly leads to the conversion reaction $FeF_6^{3-} \to FeF_4^- + 2F^-$. Therefore, to stabilize Fe–F bonds and reduce octahedral chain distortion play an important role in improving their electrochemical performance of FeF_3 cathode materials with water.

1 Introduction

Rechargeable lithium-ion batteries (LIBs) have attracted tremendous attention due to their vast potential market for electric vehicles and portal electronic devices.[1] Improving electrochemical performance of cathode materials by optimizing microstructure and tailoring composition, though very challenging, plays an important role in realizing LIB practical application with satisfactory power and energy densities as well as low cost.[2,3] Compared with layered intercalation compounds only transferring one electron at most per formula during discharge-charge cycle, transition metal fluorides based on conversion reaction in which multiple electrons can be transferred, offer a tremendous advantages in energy and power densities.[4-6] Among all M_xF_y compounds, iron trifluoride (FeF_3) is the most promising cathode material because of its superior intrinsic characteristics such as high theoretical specific capacity (712 mAh g^{-1} in the potential interval 1.5-4.5 V $vs.$ Li^+/Li), low toxicity and cost, and good thermal stability.[7-9] However, its practical application as LIB cathodes material has been severely prevented by its low electronic conductivity and sluggish kinetics closely associated with the high ionicity of Fe–F bonds.[10]

Besides FeF_3-carbon nanocomposition, structural expansion, fabricating open framework FeF_3 is considered as a possible strategy to increase ionic conductivities. Li et al. firstly synthesized FeF_3 with race amounts of water ($FeF_3 \bullet 0.33H_2O$[11] and $FeF_3 \bullet 0.5H_2O$[12]), which was demonstrated to have an improved electrochemical performances such as a larger reversible capacity and good cycle performance in voltage range 1.7-4.5 V. Such an open framework materials also provide new opportunities for Na and Mg batteries. Although the expanded structure possesses a significant potential to increase Li^+ storage capacity and to enhance Li^+ transport kinetics as compared with the poorly conductive ReO_3-type FeF_3, most electrochemical studies only concentrate on 1e$^-$ transfer with no conversion reaction involved. The excessive discharge after 1e$^-$ transfer will result in occurrence of amorphous structure from ordered framework structure. Very importantly, a wide discharge voltage window (1.6-3.4V) was presented in $FeF_3 \bullet 0.33H_2O$ and $FeF_3 \bullet 0.5H_2O$.[11,13-15] A trace amount of water accommodated in cathode materials has been reported in many publications.[16-20] However, an impact of water on electrochemical performance has not been studied so far. It is of significant importance to reveal open framework structure stability mechanism and understand electrochemical role of water.

Li et al synthesized $FeF_3 \bullet 0.33H_2O$ with a unique one-dimensional tunnel by using the low-temperature ionic-liquid-based synthesis method.[11,13,15] Its discharge capacity is measured as 153 mAh g^{-1} at the sixth cycle and decreased to 130 mAh g^{-1} after 30 cycles at a current density of 14 mA g^{-1}. The further nanocomposition materials such as $FeF_3 \bullet 0.33H_2O/SWNT$,[12] $FeF_3 \bullet 0.33H_2O/MoS_2$,[21] and $FeF_3 \bullet 0.33H_2O/V_2O_5$[22] and $FeF_3 \bullet 0.33H_2O/ACMB$ (active carbon microbead)[23] exhibited an improved rate capacity and cycle performances. However, these studies did not provide enough information on underlying mechanism in structural stability and electrochemical effect induced by water. To the best of my knowledge, no theoretical study on $FeF_3 \bullet 0.33H_2O$ is reported so far.

In this work, the first-principles calculations combining thermodynamic analysis were performed to reveal the role of water

Address here Address here. State *Key Laboratory of High Performance Ceramics and Superfine Microstructures, Shanghai Institute of Ceramics, Chinese Academy of Sciences, Shanghai 200050, China.*

in tuning structural stability and electrochemical performance of $FeF_3 \bullet 0.33H_2O$. Our calculations indicate that hydrogen bonding between H_2O and F^- can be mediated by occupied positions and amount of Li^+ ions, which directly affects discharge voltage and Li^+ transport behaviour of $Li_{0.66}FeF_3 \bullet 0.33H_2O$. We predict that stabilizing Fe–F bonds and reducing octahedral chain distortion play an important role in improving electrochemical performance of $FeF_3 \bullet 0.33H_2O$.

2 Computational Methods

The first-principles calculations were conducted within the formalism of spin-polarization density functional theory (DFT) and the generalized gradient approximation (GGA) of the exchange-correlation function as formulated by Perdew, Burke, and Ernzerhof.[24] The valence electron–ion interaction was treated by the projector augmented wave (PAW) potential[25] in the Vienna Ab initio Simulation Package (VASP).[26,27] To take into account the strong correlated character of the d-electrons of Fe, a Hubbard-like correction (GGA+U)[25,28] is used. Within the GGA+U approach, only the difference between U and J (U_{eff}=U-J) is meaningful. So an effective interaction parameter U_{eff}=5 eV was used in our calculations, which is consistent with the previous publications.[29,30] The van der Waals-augmented density functional theory (vdW-DFT) was used to modify exchange and correlation energies.[31] The functional optB88-vdW was chosen to accurately describe the behaviour of water.[32] Klimeš et al. demonstrated that the optB88-vdW could obtain more accurate vdW weak interaction energies in a variety of dispersion and hydrogen bonding systems than other exchange functionals such as optPBE-vdW and optB86b-vdW.[33] The wave functions were expanded in plane-wave basis set up to a kinetic energy cutoff of 400 eV. Brillouin-zone integrations were performed by using the k-point sampling of the Monkhorst-Pack scheme[34] with a 3×3×3 grid. The convergence of total energy with respect to the kinetic energy cutoff and the k-point sampling has been carefully examined. Minimization of the total energy was realized with a full relaxation of the atomic positions and cell parameters for each structure. According the results of experiments,[35] the iron fluoride system in this work displayed strictly noncollinear antiferromagnetic (AFM) ground states along c axis below the Néel temperature (TN) 129 K with the magnetic moments (μ= 4.07 μB).[36,37] The migration mechanisms were calculated by using the climbing image-nudged elastic band (CI-NEB),[38] which is a reliable approach to search the minimum-energy path (MEP). The electrical conductivity is calculated by means of the Kubo-Greenwood approach,[39] which is a very general formulation for the conductivity.[40] In this approach, the electrical conductivity σ can be obtained by extrapolating to zero frequency:

$$\sigma = \sigma(0) = \lim_{\omega \to 0} \sigma(\omega) \qquad (1)$$

with $\sigma(\omega)$ computed as a configurational average of

$$\sigma(\omega, R_I) = \frac{2\pi e^2}{3m^2\omega} \frac{1}{V} \sum_{i,j} (f_i - f_i) \left| \langle \psi_i | \hat{p} | \psi_j \rangle \right|^2 \delta(E_j - E_i - \hbar\omega) \qquad (2)$$

where e and m are the electronic charge and mass, $\hat{p}$ is the momentum operator and ψ_i, E_i, are the electronic DFT eigenstates and eigenvalues, calculated for the ionic configuration$\{R_I\}$, at a single k point of the Brillouin Zone.

3 Results and Discussion

3.1 Open Framework Structure Stability of $FeF_3 \bullet 0.33H_2O$

Several experimental studies[35-37,41,42] have determined that $FeF_3 \bullet 0.33H_2O$ is in a HTB (Hexagonal Tungsten Bronze) structure with space group *Cmcm* (space group 137)[13,15] and six FeF_3 perovskites are connected via corner-sharing to form a huge hexagonal cavity. The local structures of water interacting with open framework structure are difficult to be experimentally determined due to mobility of H atoms. This is directly related to the interaction between water molecules and the hexagonal cavity, even to the insertion sites and migration path of lithium ions.
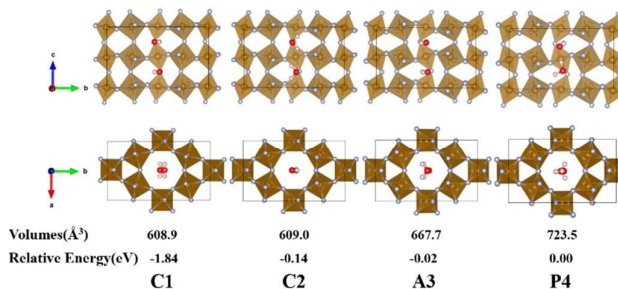

Volumes(Å³)	608.9	609.0	667.7	723.5
Relative Energy(eV)	-1.84	-0.14	-0.02	0.00
	C1	C2	A3	P4

Fig. 1 The side and top views of relaxed $FeF_3 \bullet 0.33H_2O$ structures due to different orientation of water molecules. Fe, F, O and H atoms are presented by earthy yellow, blue gray, red, and light brown balls, respectively; the relaxed cell volumes (Å³) and relative energy (eV) also are listed here.

All optimized structures and relative energies of $FeF_3 \bullet 0.33H_2O$ are shown in Fig. 1. According to relative positions of hydrogen atoms, three possible local structures of water interacting with cavity FeF_3 are considered. First of all, the hydrogen atoms of two water molecules are toward opposite directions in a unit cell. Two relaxed structures in which water molecules are in (001) and (100) planes were displayed in Fig. 1 C1 and C2, respectively. They have orthorhombic symmetry with the space group of *Cmcm.* Herein, two relaxed structures are labelled as C1 and C2 according to their corresponding space group symmetry (the first letter) combined with the order of stability, which is also applied in the other relaxed structures (A3 and P4). In these structures, hydrogen atoms occupy 8g site in C1 and 8f site in C2. Secondly, four hydrogen atoms of two water molecules point one direction along *b* axis, as shown in Fig. 1 A3. The relaxed structure displays an orthorhombic symmetry with the space group of *Amm2*. Hydrogen atoms in this structure are all in (001) plane and occupy 4d and 4e positions. Thirdly, two waters in tunnel approach each other to form a cluster structure due to strong hydrogen bonding, as shown in Fig. 1 P4. The relaxed P4 structure has a low symmetry with the space group *P1*. As shown in Fig. 1, the orthorhombic structure C1 was found to have the lowest energy and smallest cell volume in all four relaxed structures. Our calculated structure symmetry and cell volume are qualitatively consistent with experimental measurement.[13] Therefore, the C1 structure is considered in the following electrochemical calculations.

Journal of Material Chemistry A

PAPER

Table 1 The relaxed lattice parameter (Å), unit cell volumes (Å^3), the experiment data, diameter of hole (van der Waals radius of fluoride atom used 1.40 Å), and hydrogen bonding energy of each water of FeF$_3$, FeF$_3$•0.16H$_2$O, FeF$_3$•0.33H$_2$O, and FeF$_3$•0.66H$_2$O.

	FeF$_3$(S0)	FeF$_3$•0.16H$_2$O	FeF$_3$•0.33H$_2$O(Exp.[13,35])	FeF$_3$•0.66H$_2$O
a(Å)	7.15	7.16	7.43(7.42/7.42)	7.28
b(Å)	12.04	12.17	12.83(12.82/12.73)	12.59
c(Å)	7.11	7.16	7.59(7.46/7.53)	7.53
V(Å^3)	612.5	623.5	723.5(709.3/711.2)	690.6
Diameter(Å)	5.02/5.25	5.08/5.32	5.15/5.55(5.23)	5.16/5.47
Fe-F chain 1	1.92/1.90/1.90	1.91/1.90/1.88	1.94/1.93/1.92	2.03/1.99/1.92
Fe-F chain 2	1.92/1.90/1.90	1.91/1.90/1.89	1.93/1.93/1.93	1.96/1.92/1.89
E^{H-F}/H$_2$O(eV)	--	-0.37	-0.46	-1.23

By carefully observing open framework structure of FeF$_3$•0.33H$_2$O, it is found that its structural stability is affected by two factors, torsion between two connected FeF$_6$ hexagons and magnitude of waters. In order to quantitatively describe the correlation between hexagonal torsion and structural stability, energy evolution by scanning torsion angles was calculated by using FeF$_3$ with open framework structure. The relative energy change as a function of torsion angle was presented in Fig. 2 (a). First of all, the FeF$_3$ was relaxed after removing H$_2$O molecules from FeF$_3$•0.33H$_2$O. The relaxed structure marked as S0 in Fig. 2 (a) was displayed in Fig. 2 (b). Based on this structure, torsion angles (φ_1 and φ_2) between two hexagons were defined along two different chains. In S0, φ_1 and φ_2 are calculated as 22.1^o and 21.9^o. Therefore, the correlation between structural stability and torsion angles is obtained by scanning φ_1 (0°-22.1^o) and φ_2 (0°-21.9^o). It is noted that structural stability here is described by the equation of $\Delta E = E_{S_n} - E_{S_0}$ $(n = 1\sim9)$, where E_{S_n} and E_{S_0} are total energies of scanned structures and S$_0$. As shown in Fig. 2 (a), the open framework structures gradually become more unstable with increasing torsion angles between two connected hexagons.
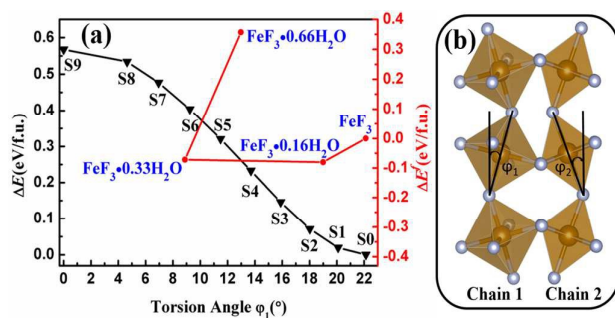

Fig. 2 (a) The relative energies (in black, labelled by S0~S9) of anhydrous FeF$_3$, and relative formation energies (in red) for FeF$_3$•nH$_2$O (n=0.00-0.66) as a function of torsion angle of Chain 1; (b) the defined torsion angles (φ_1 and φ_2) in open framework anhydrous FeF$_3$.

According to our calculations, introducing waters in lattice not only leads to torsion angle reduced, but also forms hydrogen bonding between H$_2$O and FeF$_3$. Therefore, the FeF$_3$•nH$_2$O (n=0, 0.16, 0.33 and 0.66) with different water content were calculated to reveal the relationship between stability and water content. The optimized lattice parameters and unit cell volume of different of FeF$_3$•nH$_2$O (n=0, 0.16, 0.33 and 0.66) are presented in Table 1. Our calculated lattice parameters and volumes are in good agreement with experimental measurement. Based on van der Waals radius of F atom, the diameters of two holes in FeF$_3$•0.33H$_2$O were estimated as 5.15 and 5.55 Å, which are also consistent with experimental value (5.23Å). An obvious feature with increasing water content in lattice is volume expansion by FeF$_6$ hexagonal torsion. As shown in Fig. 2, water insertion into the framework structure mitigates the torsion of the FeF$_3$ chain, which is probably originated from Jahn-Teller effect. As shown in Fig. 2(a), the reduced torsion directly leads to instability of framework structure. Particularly, the Fe–F bonds in FeF$_3$•0.33H$_2$O are elongated as comparison with those of FeF$_3$•0.16H$_2$O and FeF$_3$. On the contrary, insertion of water also enhances stability of FeF$_3$•nH$_2$O due to hydrogen bonding energies between water and F$^-$. Therefore, there exists two opposite effects in FeF$_3$•nH$_2$O due to hydrogen bonding.

It is interesting to elucidate how much hydrous water can be accommodated in one-dimension cavity in FeF$_3$. Based on the frame structure of FeF$_3$•0.33H$_2$O, the possible FeF$_3$•nH$_2$O (n=0.0, 0.16, 0.33, and 0.66) structures with the different water content were calculated. The relative formation energy ΔE^f is defined to describe the strength of hydrogen bonding according to the following equations:

$$\Delta E^f = E^f_{\text{FeF}_3 \cdot n\text{H}_2\text{O}} - E^f_{\text{FeF}_3} \tag{3}$$

$$E^f_{\text{FeF}_3 \cdot n\text{H}_2\text{O}} = E^{tot}_{\text{FeF}_3 \cdot n\text{H}_2\text{O}} - E^{\text{Fe}} - 3E^{\text{F}} - nE^{\text{H}_2\text{O}} \tag{4}$$

$$E^f_{\text{FeF}_3} = E^{tot}_{\text{FeF}_3} - E^{\text{Fe}} - 3E^{\text{F}} \tag{5}$$

where $E^f_{\text{FeF}_3 \cdot n\text{H}_2\text{O}}$ is formation energy for per FeF$_3$•nH$_2$O formula unit, $E^{tot}_{\text{FeF}_3 \cdot n\text{H}_2\text{O}}$ is the energy of per FeF$_3$•nH$_2$O formula unit, $E^{\text{H}_2\text{O}}$ is the energy of one water molecule, $E^f_{\text{FeF}_3}$ is the formation energy of per FeF$_3$ unit and $E^{tot}_{\text{FeF}_3}$ is the energy of per FeF$_3$ formula unit,

while ΔE^f represent stability change of per FeF_3 unit after hydrous water insertion. The calculated formation energies, hydrogen bonding energies, and relative energies with water content change were displayed in Fig. 2 (a). In comparison, $FeF_3 \bullet 0.16H_2O$ and $FeF_3 \bullet 0.33H_2O$ are found to have lower formation energy than FeF_3 and $FeF_3 \bullet 0.66H_2O$, indicating $FeF_3 \bullet 0.16H_2O$ and $FeF_3 \bullet 0.33H_2O$ is very likely to be experimentally observed.
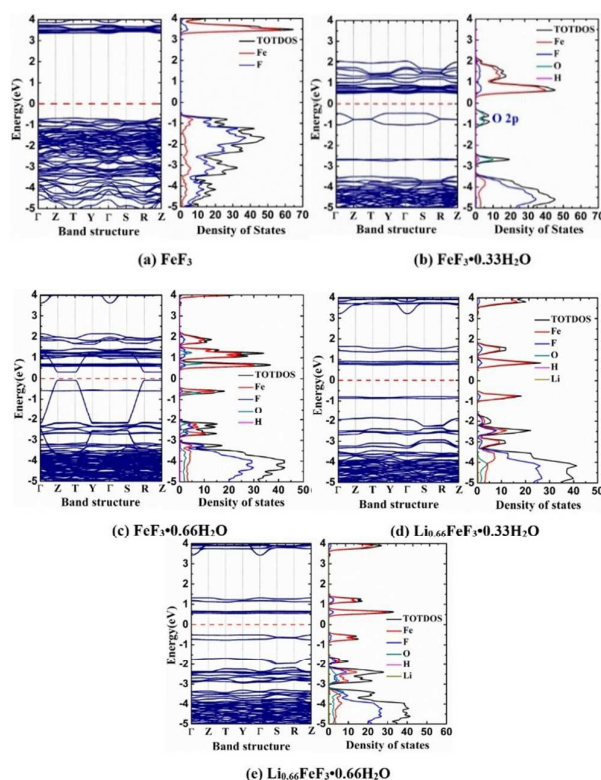

Fig. 3 The band structure and density of states (total and partial DOS, TOTDOS and PDOS) of FeF_3, $FeF_3 \bullet 0.33H_2O$, $FeF_3 \bullet 0.66H_2O$, $Li_{0.66}FeF_3 \bullet 0.33H_2O$ and $Li_{0.66}FeF_3 \bullet 0.66H_2O$. All energies are relative to the Fermi energies respectively (red dot line).

3.2 Electronic and Magnetic Properties of $FeF_3 \bullet 0.33H_2O$

Both electronic structure properties of FeF_3 and $FeF_3 \bullet 0.33H_2O$ have been calculated by GGA+U method for comparison. Their band structures and the corresponding density of states (DOS) are shown in Fig. 3. Iron fluoride is a standard ionic crystal with a large band gap width. By using PBE functional, the band gap of FeF_3 with open framework structure is calculated as 4.01 eV which is slightly smaller than that of bulk FeF_3 (4.3 eV).[30] The electronic structure change induced by microscopic structure change may lead to a significant improvement on electrochemical properties. The band gap of $FeF_3 \bullet 0.33H_2O$ can be further reduced to 0.95 eV because of an intermediate band with the main O-2p character. The insulting FeF_3 turns into some characteristics of semiconductor due to the introduction of intermediate band. The electron transition from valence band to intermediate band is easier than to conduction band. This situation is similar to solar cell in which the intermediate band is designed to favour electron transition.[43] In this framework,

the intermediate band could improve conductivity in an electrochemical condition.

With the water concentration increased, the band gap of $FeF_3 \bullet nH_2O$ becomes smaller, changing from 0.95 eV in $FeF_3 \bullet 0.33H_2O$ to 0.39 eV in $FeF_3 \bullet 0.66H_2O$. When Li ions are inserted in the hole, the band gaps of $Li_{0.66}FeF_3 \bullet 0.33H_2O$ and $Li_{0.66}FeF_3 \bullet 0.66H_2O$ are increased to 1.53 eV and 1.04 eV, respectively. Based on the Kubo-Greenwoord formula, the electric conductivities of $FeF_3 \bullet 0.33H_2O$ (7.0×10^{-8} S cm^{-1}), $Li_{0.66}FeF_3 \bullet 0.33H_2O$ (1.0×10^{-9} S cm^{-1}), $FeF_3 \bullet 0.66H_2O$ (2.8×10^{-7} S cm^{-1}) and $Li_{0.66}FeF_3 \bullet 0.66H_2O$ (7.0×10^{-8} S cm^{-1}) were calculated to evaluate the electron transport property as cathode materials. Our calculated value for $FeF_3 \bullet 0.33H_2O$ is in excellent agreement with the experimental result (1.4×10^{-8} S cm^{-1}) measured by Li et al.[13] In general, the order of electronic conductivity is accordance with the band gap. Because the band gap is increased with Li^+ insertion, the electric conductivity of $Li_{0.66}FeF_3 \bullet 0.33H_2O$ is significantly reduced, which is a possible reason for relatively high overpotential (0.4-0.5 eV) in experiment. As a result, tailoring band gap of $Li_{0.66}FeF_3 \bullet 0.33H_2O$ plays an important role in reducing charging voltage.

FeF_3 crystal with HTB (Hexagonal Tungsten Bronze) structure undergoes long-range ordering to a noncollinear antiferromagnetic G-type structure, which has been observed experimentally.[35] The predicted total magnetic moments of Fe in $FeF_3 \bullet 0.33H_2O$ is about 4.48 μB which agrees reasonably well with experimental data 4.07 μB.[35] The spin direction of three magnetic sublattices is at 120° one from each other in each 001 plane.
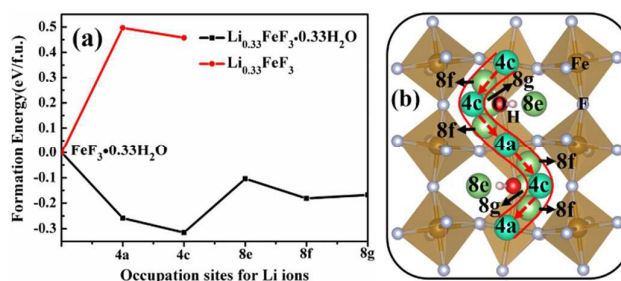

Fig. 4 (a) The formation energy of a single Li^+ insertion at different Wyckoff positions in anhydrous FeF_3 (in red) and $FeF_3 \bullet 0.33H_2O$ (in black); (b) the different Wyckoff positions are presented. The low-energy 4a and 4c positions are described in the dark green balls. The high-energy 8e, 8f, and 8g positions are described in the light green balls.

3.3 Li^+ Insertion into $FeF_3 \bullet 0.33H_2O$

As mentioned above, the crystal structure of $FeF_3 \bullet 0.33H_2O$ belongs to space group *Cmcm* with orthorhombic symmetric structure. The wall of hexagonal cavity consists of fluoride atoms while the water molecules are alternately arranged in opposite directions. Except water and FeF_3 octahedral, the symmetrically distinct sites for Li ions insertion are only possible at Wyckoff position as 4a, 4c, 8e, 8f and 8g. 4c and 8e sites are all in the perpendicular bisecting plane. 4c is on the side of oxygen atom, while 8e is on the side of hydrogen atoms. 4a is at the middle point of every two adjacent oxygen atoms. 8f is at the middle point between 4a and 4c. 8g and water

ARTICLE

molecule are in the same plane and 8g is contrary to the hydrogen atom position, relative to the oxygen atom.

The site preference for inserted Li^+ was investigated in a dilute approximation by calculating energy change of inserting a single Li^+ in the possible distinct binding sites. The formation energies in which $FeF_3 \cdot 0.33H_2O$ was used as a reference state were calculated and displayed in Fig. 4 (a). According to formation energy of Li ions insertion, the insertion positions in fully lithiated $Li_{0.66}FeF_3 \cdot 0.33H_2O$ should be at 4c due to the lowest formation energy at the dilute limit. In order to reveal the possible effect of water on Li^+ insertion, the possible lower-energy site position of Li^+ in FeF_3 was calculated by considering 4a and 4c positions. As shown in Fig. 4 (b), the 4c position is the most stable insertion site for Li ion, regardless of whether there is water molecule in channel.

In order to estimate the structural stability associated with Li^+ concentration, the cohesive energies ($\Delta E^f = E_{Li_xFeF_3 \cdot 0.33H_2O} - E_{Li^+} - E_{Fe} - E_{0.5F_2} - E_{0.33H_2O}$) of Li^+ inserted into the cavity structure of $FeF_3 \cdot 0.33H_2O$ were calculated. The relative cohesive energies with a change of Li^+ concentration were displayed in Fig. 5 (a). The relaxed $Li_xFeF_3 \cdot 0.33H_2O$ (x=0.0, 0.33, 0.50, 0.66, 0.83, and 1.00) structures also were presented in Fig. 5 (a) to describe structural change induced by Li^+ insertion. Obviously, the cohesive energies of Li^+ in the cavity are gradually decreased with increasing Li^+ concentration. Interestingly, our calculations showed that the maximum capacity of Li^+ under maintaining the $FeF_3 \cdot 0.33H_2O$ cavity structure may be 0.66, reaching the most stable species of $Li_{0.66}FeF_3 \cdot 0.33H_2O$. This calculated result is qualitatively consistent with the experimental measurement. When more Li^+ ions are inserted after $Li_{0.66}FeF_3 \cdot 0.33H_2O$, an octahedral chain (Chain 1 in Fig. 2) undergo transition from octahedral structure (FeF_6^{3-}) to tetrahedral structure (FeF_4^-) and LiF, describing as the conversion reaction of $Li_3FeF_6 \rightarrow LiFeF_4 + 2LiF$. It indicates that a slightly excessive discharge may lead to a significant structure change and therefore should be avoided in the practical operation.
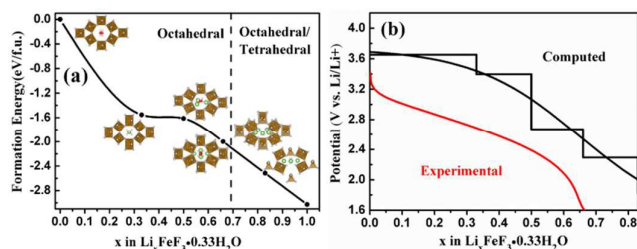

Fig. 5 (a) The relative formation energy and structural transition with Li+ concentration change of $Li_xFeF_3 \cdot 0.33H_2O$ ($0.0 \leq x \leq 1.0$). From x=0.66 to x=0.83, the octahedral FeF_6^{3-} undergoes structural transition to tetrahedral FeF_4^- and $2F^-$; (b) the calculated voltage plateaus of $Li_xFeF_3 \cdot 0.33H_2O$ and fitted voltage curve (in black) and the experimental discharge potential profile for comparison.[13]

To describe quantitatively such a structural transition and its mechanism, the primitive cell volumes (V), bond lengths of Fe–F (r_{Fe-F}), and Bader charges of Fe ions were presented in Table 2 for comparison. First of all, the Li^+ insertion leads to a significant volume shrinkage. The structural analysis shows that Li^+ insertion directly induces decreasing torsion angles of octahedral chains

probably due to a weakened hydrogen bonding between H_2O and F^-. The torsion angles of Chain 1 and Chain 2 in $FeF_3 \cdot 0.33H_2O \rightarrow Li_{0.33}FeF_3 \cdot 0.33H_2O \rightarrow Li_{0.66}FeF_3 \cdot 0.33H_2O$ are calculated as $9.8^o \rightarrow 19.1^o \rightarrow 21.1^o$ and $9.8^o \rightarrow 17.5^o \rightarrow 19.5^o$, respectively. Hydrogen bonding strength is reduced from -0.46 eV in $FeF_3 \cdot 0.33H_2O$ to -0.01 eV in $Li_{0.66}FeF_3 \cdot 0.33H_2O$. This indicates that Li^+ insertion introduces electrostatic interaction of Li^+-F^- and Li^+-H_2O pairs. In meanwhile, hydrogen bonding strength of F^--H_2O is reduced with increasing Li^+ concentration. The distortion of octahedral chains might directly result the shrinkage of lattice constants and volumes. The unit cell volume change during the charge/discharge processes is 8.3%, which rather comparable to that of $LiFePO_4$ (6.5%).[44] Actually, a similar situation also appears in other open framework battery material.[45]

Table 2 The unit cell volumes ($\mathring{A}^3$), average bond length of Fe–F (r_{Fe-F}, $\mathring{A}$), and Bader charge (c_{Fe}, in bracket) of Fe in Chain 1 and Chain 2 as shown in Fig. 2.

Species	$V(\mathring{A}^3)$	r_{Fe-F} and c_{Fe} in Chain 1	r_{Fe-F} and c_{Fe} in Chain 2
$FeF_3 \cdot 0.33H_2O$	361.8	1.93 (+2.0)	1.93 (+2.0)
$Li_{0.33}FeF_3 \cdot 0.33H_2O$	314.6	2.03 (+1.9/+1.5)	1.89 (+1.9)
$Li_{0.5}FeF_3 \cdot 0.33H_2O$	325.9	2.01(+1.9/+1.5)	1.90 (+1.9)
$Li_{0.66}FeF_3 \cdot 0.33H_2O$	331.6	2.01 (+1.5)	1.91 (+1.9)
$Li_{0.83}FeF_3 \cdot 0.33H_2O$	348.1	2.03 (+1.5)	2.48 (+1.9/+1.5)
$LiFeF_3 \cdot 0.33H_2O$	356.8	2.02 (+1.4)	2.66 (+1.5)

Further, the structural transition associated with the conversion reaction of $Li_3FeF_6 \rightarrow LiFeF_4 + 2LiF$ can be characterized by the bond length change of Fe–F as shown in Table 2. From $FeF_3 \cdot 0.33H_2O$ to $LiFeF_3 \cdot 0.33H_2O$, the bond lengths of Fe–F in Chain 1 are not changed too much, whereas those in Chain 2 have a sharp stretching from 1.91Å ($Li_{0.66}FeF_3 \cdot 0.33H_2O$) to 2.48 Å ($Li_{0.83}FeF_3 \cdot 0.33H_2O$). Our Bader charge analysis indicates that such a structural transition is closely associated with the charge state of Fe ion. The charge state change from +3 to +2 directly induces the bond stretching of Fe–F in Chain 1. In contrast, the similar charge change from $FeF_3 \cdot 0.33H_2O$ to $Li_{0.33}FeF_3 \cdot 0.33H_2O$ does not lead to the bond elongation. Therefore, it is predicted that enhancing bond strength of Fe–F in Chain 2 plays an important role in increasing Li^+ storage capacity.

Based on our thermodynamic calculations, it is very necessary to further calculate the intercalation/deintercalation voltage of cell in comparison with experimental measurement. For any intercalation system, the total Gibbs free energy change can be written as:

$$dG = -SdT + VdP + \mu_{Li}N_{Li} + \mu_{FeF_3 \cdot 0.33H_2O}dN_{FeF_3 \cdot 0.33H_2O} \quad (6)$$

where G is the Gibbs free energy, S is the entropy, T is the temperature, V is the volume, P is the pressure, μ_{Li} and N_{Li} are the chemical potential and amount of electrode materials, respectively. When the operating temperature and pressure are kept constant, the equation (4) can be simplified as $dG = \mu_{Li}dN_{Li}$. Therefore, the chemical potential of Li^+ further can be written as $\mu_{Li} = dG/dN_{Li}$. According to the Nernst equation, the voltage of cell can be expressed as $V^{cell} = -(\mu_{Li}^{cathode} - \mu_{Li}^{anode})/Ze$, where Z is the valence (+1) of Li^+. With the reference of anode material (Li metal), the voltage thus is calculated according to the following formula:

$$V^{cell} = -(G_{Li_{x+n}FeF_3 \cdot 0.33H_2O} - G_{Li_xFeF_3 \cdot 0.33H_2O} - G_{nLi})/n \quad (7)$$

The calculated intercalation/deintercalation voltage plateaus of $Li_xFeF_3 \cdot 0.33H_2O$ were displayed in Fig. 5 (b). For comparison, the experimental discharge voltage also were presented here. The calculated voltages have a wide window from 3.6 to 2.2 V, which is probably ascribed to electrostatic interaction between Li^+ and H_2O, as well as FeF_3 structure change due to $H_2O \cdots F^-$ hydrogen bonding. As shown in Fig. 5 (b), our calculated voltages are about 0.2 V higher than the corresponding experimental values. The overestimation may be attributed to the battery internal resistance and calculation errors.

3.4 Li^+ Transportation Mechanisms

The CI-NEB and DFT methods have been successfully applied to determine lithium migration paths and energy barriers for electrode materials.[46,47] Both knock-off migration and cooperative migration mechanisms were investigated in solid-state electrode and electrolyte materials. The typical knock-off mechanism is an asynchronous migration process in which Li^+ migrates into a neighboring vacancy followed by nearby Li^+ further migrates into the newly-generated vacancy. In contrast, the cooperative mechanism presents a synchronous migration mode in which the nearby Li^+ ions replaced one another. In this work, the CI-NEB method based on DFT-PBE was used to calculate reaction paths of Li^+ transportation considering the possible knock-off migration and cooperative migration mechanisms. In terms of knock-off migration mechanism, a Li^+ vacancy is generated at 4a position which has a higher site energy than 4c position. It is predicted that lithium ions occupying 4a and 4c positions in tunnel follow a zigzag path around water molecules along c axis direction. The energy profiles of two Li^+ transportation paths are displayed in Fig. 6. In order to reveal the detailed transportation mechanism, all transition state and minimum structures with emphasis on H_2O-Li^+ interaction are also given. It is noted that our NEB calculations include all atoms in the calculated $Li_{0.66}FeF_3 \cdot 0.33H_2O$ lattice.
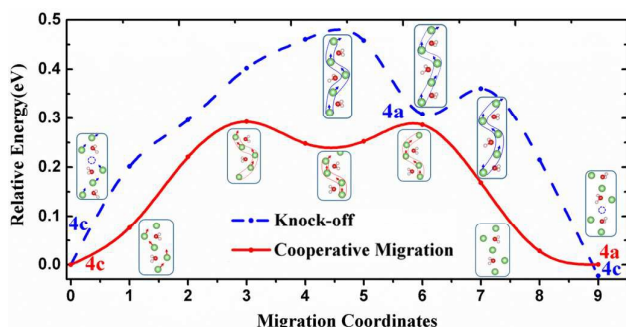

Fig. 6 The CI-NEB-calculated potential energy curves of Li^+ migration paths. The Li^+ knock-off and cooperative migration mechanisms are considered in our calculations.

It is obvious that the cooperative transportation mechanism has a lower transition state energy than the knock-off transportation mechanism. For the former, two transition states are symmetric and have the same relative energy of 0.29 eV as compared with the initial minimum structure. This process can be described as stepwise migration of Li^+ ions from 4a and 4c positions to 8f positions. Based on position preference calculations in Fig. 4 (a), it is found that 4Li^+ ions migrations from 4a/4c position to 8f position require surmounting an energy barrier of 0.44 eV. Correspondingly F^--H_2O hydrogen bonding strengths in 4a/4c and 8f positions are calculated as -0.01 and -0.14 eV, respectively. This indicates that the mediated F^--H_2O hydrogen bonding effectively reduce Li^+ migration barrier. Therefore, the electrostatic attraction between Li ions and H_2O play an important in fast ionic transportation. A relatively low transition state energy of Li^+ transportation indicates that $Li_{0.66}FeF_3 \cdot 0.33H_2O$ has a good electrochemical performance with a fast charging/discharging rate. In contrast, the knock-off mechanism has the activation barrier of 0.46 eV.

4 Conclusions

The DFT-based first-principles calculations were carried out to study the impact of water on structural stability and electrochemical performance of $Li_{0.66}FeF_3 \cdot 0.33H_2O$ as cathode material. The water molecules are isolated in the tunnels and form strong hydrogen bonding with F^- ions, which directly results in octahedral FeF_6^{3-} distortion and destabilizes FeF_3 framework structure. The most stable species are predicted as $FeF_3 \cdot nH_2O$ (n=0.16-0.33). Li^+ insertion into water-accommodated tunnel further changes torsion angle of FeF_6^{3-} octahedral chains, leading to a wide discharge voltage window of 2.2-3.6V. The species of $Li_{0.66}FeF_3 \cdot 0.33H_2O$ is the most stable with the maximum amount of Li^+ ions. More Li^+ insertion leads to the Fe–F bond cleavage and occurrence of conversion reaction of $FeF_6^{3-} \rightarrow FeF_4^- + 2F^-$. As a result, to stabilize Fe–F bonds and reduce octahedral chains by mediating hydrogen bonding play an important role in improving the electrochemical performance of $FeF_3 \cdot nH_2O$ materials.

References

1. L. W. Ji, Z. Lin, M. Alcoutlabi and X. W. Zhang, *Energy Environ. Sci.,* 2011, **4**, 2682.
2. P. G. Bruce, B. Scrosati and J. M. Tarascon, *Angew. Chem. Int. Ed.,* 2008, **47**, 2930.
3. Y. Wang and G. Z. Cao, *Adv. Mater.,* 2008, **20**, 2251.
4. J. Cabana, L. Monconduit, D. Larcher and M. R. Palacin, *Adv. Mater.,* 2010, **22**, E170.
5. Y. M. Chen, Z. G. Lu, L. M. Zhou, Y. W. Mai and H. T. Huang, *Energy Environ. Sci.,* 2012, **5**, 7898.
6. P. Poizot, S. Laruelle, S. Grugeon, L. Dupont and J. M. Tarascon, *Nature,* 2000, **407**, 496.

7. G. G. Amatucci and N. Pereira, *J. Fluorine Chem.,* 2007, **128**, 243.

8. M. J. Zhou, L. W. Zhao, T. Doi, S. Okada and J. Yamaki, *J. Power Sources,* 2010, **195**, 4952.

9. F. Badway, F. Cosandey, N. Pereira and G. G. Amatucci, *J. Electrochem. Soc.,* 2003, **150**, A1318.

10. T. Li, L. Li, Y. L. Cao, X. P. Ai and H. X. Yang, *J. Phys. Chem. C,* 2010, **114**, 3190.

11. C. Li, L. Gu, S. Tsukimoto, P. A. van Aken and J. Maier, *Adv. Mater.,* 2010, **22**, 3650.

12. C. Li, L. Gu, J. Tong, J. Maier, *ACS Nano,* 2011, **5**, 2930.

13. C. L. Li, L. Gu, J. W. Tong, S. Tsukimoto and J. Maier, *Adv. Funct. Mater.,* 2011, **21**, 1391.

14. C. Li, C. Yin, L. Gu, R. E. Dinnebier, X. Mu, P. A. van Aken and J. Maier, *J. Am. Chem. Soc.,* 2013, **135**, 11425.

15. C. L. Li, C. L. Yin, X. K. Mu and J. Maier, *Chem. Mater.,* 2013, **25**, 962.

16. Y. Wang, K. Takahashi, K. H. Lee and G. Z. Cao, *Adv. Funct. Mater.,* 2006, **16**, 1133.

17. G. Nagaraju, S. Sarkar, J. Dupont and S. Sampath, *Solid State Ionics,* 2012, **227**, 30.

18. H. Wang, W. Wang, Y. Ren, K. Huang and S. Liu, *J. Power Sources,* 2012, **199**, 263.

19. K. Wu, L. Shao, X. Jiang, M. Shui, R. Ma, M. Lao, X. Lin, D. Wang, N. Long, Y. Ren and J. Shu, *J. Power Sources,* 2014, **254**, 88.

20. F. Feng, W. Kang, F. Yu, H. Zhang and Q. Shen, *J. Power Sources,* 2015, **282**, 109.

21. R. Ma, Y. Dong, L. Xi, S. Yang, Z. Lu and C. Chung, *ACS Appl. Mat. Interfaces,* 2013, **5**, 892.

22. W. Wu, Y. Wang, X. Wang, Q. Chen, X. Wang, S. Yang, X. Liu, J. Guo and Z. Yang, *J. Alloys Compd.,* 2009, **486**, 93.

23. L. Liu, M. Zhou, X. Wang, Z. Yang, F. Tian and X. Wang, *J. Mater. Sci.,* 2011, **47**, 1819.

24. J. P. Perdew, K. Burke and M. Ernzerhof, *Phys. Rev. Lett.,* 1997, **78**, 1396.

25. J. P. Perdew, K. A. Jackson, M. R. Pederson, D. J. Singh and C. Fiolhais, *Phys. Rev. B,* 1992, **46**, 6671.

26. G. Kresse, *Phys. Rev. B,* 1996, **54**, 11169.

27. G. Kresse and J. Furthmüller, *Comput. Mater. Sci.,* 1996, **6**, 15.

28. S. L. Dudarev, S. Y. Savrasov, C. J. Humphreys and A. P. Sutton, *Phys. Rev. B,* 1998, **57**, 1505.

29. Z. Yang, Z. Huang, L. Ye and X. Xie, *Phys. Rev. B,* 1999, **60**, 15674.

30. R. F. Li, S. Q. Wu, Y. Yang and Z. Z. Zhu, *J. Phys. Chem. C,* 2010, **114**, 16813.

31. S. Savasta, O. Di Stefano, V. Savona and W. Langbein, *Phys. Rev. Lett.,* 2005, **94**, 246401.

32. M. Forster, R. Raval, J. Carrasco, A. Michaelides and A. Hodgson, *Chem. Sci.,* 2012, **3**, 93.

33. J. Klimes, D. R. Bowler and A. Michaelides, *J. Phys. Condens. Matter,* 2010, **22**, 022201.

34. H. J. Monkhorst and J. D. Pack, *Phys. Rev. B,* 1976, **13**, 5188.

35. M. Leblanc, R. De Pape, G. Ferey and J. Pannetier, *Solid State Commun.,* 1986, **58**, 171.

36. M. Leblanc, G. Ferey, P. Chevallier, Y. Calage and R. De Pape, *J. Solid State Chem.,* 1983, **47**, 53.

37. Y. Calage, M. Leblanc, G. Ferey and F. Varret, *J. Magn. Magn. Mater.,* 1984, **43**, 195.

38. G. Henkelman, B. P. Uberuaga and H. Jonsson, *J. Chem. Phys.,* 2000, **113**, 9901.

39. D. A. Greenwood, *Proc. Phys. Soc.,* 1958, **71**, 585.

40. P. L. Silvestrelli, *Phys. Rev. B,* 1999, **60**, 16382.

41. G. Teufer, *Acta Cryst.,* 1964, **17**, 1480.

42. D. Leduje and J. Teillet, *Phys. Status Solidi B,* 1993, **179**, 201.

43. A. Martí, E. Antolín, C. R. Stanley, C. D. Farmer, N. López, P. Díaz, E. Cánovas, P. G. Linares and A. Luque, *Phys. Rev. Lett.,* 2006, **97**, 247701.

44. A. K. Padhi, *J. Electrochem. Soc.,* 1997, **144**, 1188.

45. M. Okubo, D. Asakura, Y. Mizuno, J. D. Kim, T. Mizokawa, T. Kudo and I. Honma, *J. Phys. Chem. Lett.,* 2010, **1**, 2063.

46. D. Su, H. Ahn and G. Wang, *Appl. Phys. Lett.,* 2011, **99**, 141909.

47. C. H. Hu, Z. Q. Wang, Z. Y. Sun and C. Y. Ouyang, *Chem. Phys. Lett.,* 2014, **591**, 16.

Graphical Abstract

The tunable H_2O-F^- hydrogen bonding is crucial to structural stability and electrochemical performance of $FeF_3 \cdot 0.33H_2O$ cathode material.